Solar Energy 309 (2026) 114430

Contents lists available at ScienceDirect

Solar Energy

journal homepage: www.elsevier.com/locate/solener

Synergistic preheating and moderate temperature liquid medium annealing for high performance perovskite solar cells

Wei-Hao Chiu [a], Wei-Lun Yu [b], Ming-Chung Wu [a,c,d], Jen-Fu Hsu [d,e], Gao Chen [f], Ching-Yuan Liu [b,*], Kun-Mu Lee [a,c,d,g,**]

[a] Center for Sustainability and Energy Technologies, Chang Gung University, Taoyuan 33302, Taiwan
[b] Department of Chemical and Materials Engineering, National Central University, Taoyua 32001, Taiwan
[c] Department of Chemical and Materials Engineering, Chang Gung University, Taoyuan 33302, Taiwan
[d] Division of Neonatology, Department of Pediatrics, Chang Gung Memorial Hospital, Taoyuan 33305, Taiwan
[e] School of Medicine, College of Medicine, Chang Gung University, Taoyuan 33302, Taiwan
[f] Department of Applied Physics, The Hong Kong Polytechnic University, Hung Hom, Kowloon, Hong Kong 999077, PR China
[g] College of Environment and Resources, Ming Chi University of Technology, New Taipei City 24301, Taiwan

ARTICLE INFO

Keywords:
FABr passivation
Halide perovskite
Liquid medium annealing (LMA)
Pre-heat treatment

ABSTRACT

The performance and stability of perovskite solar cells (PSCs) can be limited by film quality and interfacial defects. In this study, we developed a moderate-temperature liquid medium annealing (LMA) process that involves a 20-s preheating step, followed by formamidinium bromide (FABr) passivation. The preheating step effectively removes residual antisolvent and initiates uniform nucleation, enabling the formation of continuous and uniform perovskite films with large grains and high crystallinity. The optimal time and temperature for LMA were determined to be 3 min and 50 °C, respectively. Devices fabricated through LMA involving the preheating step exhibited a champion power conversion efficiency (PCE) of 21.49% and suppressed hysteresis. Incorporation of FABr passivation into this process improved the PCE to 22.01%, reduced the trap density between perovskite and the hole transport material, and extended carrier lifetime. Notably, an unencapsulated PSC with perovskite films produced through LMA, preheating, and FABr passivation retained 94.5% of its initial PCE after 650 h under ISOS-D1 testing. Overall, the proposed synergistic strategy offers a scalable route for fabricating efficient and durable PSCs.

1. Introduction

Halide perovskite solar cells (PSCs) have attracted considerable attention in photovoltaic research because of their excellent optoelectronic properties, strong light absorption, high power conversion efficiencies (PCEs), and tunable bandgaps [1–4]. When first introduced in 2009, PSCs exhibited a modest PCE of only 3.8% [5]. However, they have since been confirmed to have PCEs surpassing 26%, highlighting their extraordinary potential for next-generation solar technologies [6–8]. The efficiency of PSCs is strongly influenced by film quality. The perovskite films of these cells are deposited by spin-coating a precursor solution onto a substrate and then inducing crystallization through optimized annealing methods.

One method for crystallizing perovskite involves direct hot plate annealing (HPA) of a substrate following spin-coating of a precursor solution on it. This method is widely adopted because of its convenience and simplicity [9]. Researchers have indicated that annealing time and temperature strongly influence the crystallinity and quality of perovskite films produced through HPA [10]. The primary disadvantages of HPA include high energy consumption due to its elevated temperature requirements, inadequate control over material defects, and poor process reproducibility, all of which contribute to its unsuitability for rapid, high-throughput manufacturing. These limitations can be overcome by employing electromagnetic wave techniques, such as flash lamp annealing. This method enables millisecond-scale crystallization, which is suitable for high-throughput, large-area manufacturing. It also exhibits high energy efficiency and compatibility with flexible substrates because of its minimal heating requirements [11]. However, flash lamp annealing can result in nonuniform crystal growth and requires

* Corresponding author.
** Corresponding author at: Center for Sustainability and Energy Technologies, Chang Gung University, Taoyuan 33302, Taiwan.
E-mail addresses: cyliu0312@ncu.edu.tw (C.-Y. Liu), kmlee@mail.cgu.edu.tw (K.-M. Lee).

https://doi.org/10.1016/j.solener.2026.114430
Received 10 September 2025; Received in revised form 10 February 2026; Accepted 12 February 2026
Available online 24 February 2026

Nomenclature

Symbols

A1	pre-exponential factor (amplitude) corresponding to the fast decay component in the biexponential fitting of TRPL
A2	pre-exponential factor (amplitude) corresponding to the slow decay component in the biexponential fitting of TRPL
I(t)	photoluminescence intensity at time *t* obtained from TRPL measurement
J_{SC}	short-circuit current density
PCE_{FS}	power conversion efficiency of forward scan
PCE_{RS}	power conversion efficiency of reversed scan
V_{OC}	open-circuit voltage
V_{TFL}	trap-filled limit voltage
τ_1	fast decay lifetime associated with trap-assisted nonradiative recombination in TRPL
τ_2	slow decay lifetime associated with radiative recombination in TRPL
τ_{avg}	average carrier lifetime of TRPL measurement

Abbreviations

2D	two-dimensional
CBD	chemical bath deposition
DI	deionized
EL	electroluminescence
ETL	electron transport layer
EQE	external quantum efficiency
FF	fill factor
FS	forward scan
FTO	fluorine-doped tin oxide
FWHM	full width at half maximum
HI	hysteresis index
HPA	hot plate annealing
HTL	hole transport layer
ISOS	International Summit on Organic Photovoltaic Stability
LED	light-emitting diode
LMA	liquid medium annealing
NA	numerical aperture
PCBM	phenyl-C61-butyric acid methyl ester
PCE	power conversion efficiency
PL	photoluminescence
PVSK	perovskite
PSC	perovskite solar cell
RH	relative humidity
RS	reversed scan
SCLC	space-charge limited current
SEM	scanning electron microscopy
TRPL	time-resolved photoluminescence
XRD	X-ray diffraction

specialized, costly equipment [9].

Vacuum-assisted annealing can improve the uniformity of perovskite films by reducing ambient pressure, which enables the efficient and homogeneous removal of volatile by-products during crystallization [12,13]. This process results in films with large surface coverage and substantially enhances the long-term stability of perovskite devices in air. However, it requires additional vacuum equipment, which increases the complexity and cost of manufacturing. High-pressure annealing modifies crystal growth kinetics to produce films with larger grains, higher crystallinity, and stronger light absorption compared with those produced through vacuum-assisted annealing [14]. This low-pressure technique allows for the fabrication of devices with excellent stability that are capable of retaining high efficiency even after prolonged exposure to heat and humidity.

In addition to vacuum-assisted methods, liquid medium annealing (LMA) are innovative approaches that can be used for the commercial fabrication of PSCs. In LMA, a hot liquid medium, such as anisole, is used to anneal perovskite films [15]. The core advantage of LMA lies in its ability to offer a considerably stable and uniform thermal field, which ensures rapid and even heat transfer across the entire substrate. This optimized thermal environment accelerates the extraction of residual solvents such as dimethyl sulfoxide (DMSO) and promotes faster, more complete conversion into the final perovskite crystal structure [15]. Furthermore, the liquid medium effectively suppresses the volatilization of crucial organic components, such as methylammonium (MA^+), thereby preventing a decline in film quality and ensuring stoichiometric accuracy. Another advantage of LMA is its excellent process reproducibility. Specifically, the method exhibits negligible sensitivity to variations in device size or ambient humidity across different environmental conditions, providing a robust and scalable pathway for the commercial fabrication of PSCs.

After a well-crystalline perovskite film deposition, serval molecules have been developed as passivation materials being utilized interlayers at the interfaces. [16,17]. Ammonium halides with long alkyl or phenyl chain, such as phenethylammonium iodide (PEAI) [18,19], phenylpropylammonium iodide (PPAI) [20], n-octylammonium halides (OAI or OABr) [21], and etc., have become popular candidates as passivation materials due to its ability to passivate defects on the surface and inhibit ion migration. However, the primary focus of this grant effort must be directed toward the demanding tasks of novel molecule design and advanced material synthesis. Mixed-salt passivation strategy, such as FABr, proposed by several researchers [22]. This approach offers an alternative strategy which leverages the individual advantages of each component while achieving an enhanced synergistic effect through their combination [23].

In this study, we combined a short-duration (3 min), moderate-temperature (50 °C) LMA process with a critical 20-s preheating step to enhance perovskite film quality, enlarge the grain size, and reduce defects at grain boundaries. Specifically, the crucial pre-heating step eliminates solvent residue and moderate-temperature and short-duration LMA achieve uniform nucleation and energy saving process. We then introduced formamidinium bromide (FABr) into the aforementioned process to passivate the interface between the perovskite layer and the hole transport material. This synergistic strategy systematically improves the structural and optoelectronic properties of the perovskite active layer. By optimizing annealing conditions and passivating residual defects, we developed PSCs with high efficiency and stability.

2. Results and discussion

LMA offers a more controlled crystallization environment than does conventional HPA. This enhanced control is primarily attributable to the omnidirectional heating characteristics of LMA, which enhance the homogeneity of the thermal distribution across the substrate and the developing perovskite film, thereby enhancing overall film uniformity. Such uniform thermal distribution is crucial because it effectively minimizes adverse temperature gradients across the entire perovskite film, which substantially reduces localized thermal stress and hinders the formation of crystalline defects. Consequently, the overall morphological and crystallographic quality of the perovskite active layer considerably improve. However, the nuanced interplay among LMA temperature and preheating parameters determines the performance of fabricated PSCs. Therefore, precise tuning of these conditions is essential

for achieving an optimal balance among efficiency, stability, and manufacturability. Consequently, this study conducted a systematic investigation into the aforementioned parameters. After these parameters were optimized, we used FABr to passivate residual surface defects and maximize the efficiency and stability of PSCs. Anisole was used as the heating medium for LMA in this study.

To gain an in-depth understanding of the mechanisms responsible for the variations in the performance of the fabricated PSCs, we performed morphological and structural characterizations of the perovskite films prepared under various conditions. Fig. 1(a)–(c) presents top-view scanning electron microscopy (SEM) images of the surface morphology of perovskite films produced through HPA, LMA without preheating, and LMA with preheating, respectively. The perovskite film fabricated through HPA [Fig. 1(a)] exhibited a relatively uniform granular structure. By contrast, the perovskite film prepared through LMA without preheating [Fig. 1(b)] exhibited a nonuniform and discontinuous morphology. The surface of this film was characterized by poorly connected, island-like domains, leading to an overall disordered structure with poor surface coverage. This distinctive morphology strongly suggests incomplete antisolvent removal, consistent with the obtained photoluminescence (PL) mapping data (Fig. 2), which reveal patterns resembling antisolvent droplets. Such an irregular film structure resulted in high grain boundary density, which adversely affected charge transport and recombination dynamics [24,25]. Consequently, the PSC fabricated through LMA without preheating exhibited the lowest PCE and most variable performance among all fabricated PSCs (Fig. 4). The perovskite film prepared through LMA at 50 °C, followed by preheating for 20 s at 135 °C [Fig. 1(c)], revealed a remarkably uniform and densely packed morphology with large and well-defined grains. This morphology is indicative of a high-quality film with low defect density [26,27], which enabled the fabrication of a PSC with strong photovoltaic performance [28,29].

Further structural insights were obtained through X-ray diffraction (XRD) analysis, [Fig. 1(d) and 1(f)]; detailed XRD data are presented in Tables S1 and S2. Fig. 1(d) depicts the XRD patterns of perovskite films processed through HPA and through LMA at various temperatures (5, 25, 50, 90, and 150 °C) with 20-s preheating at 135 °C. Additionally, Fig. 1(f) illustrates the XRD patterns of perovskite films prepared through HPA and through LMA at 50 °C with preheating for different durations (0 s, 5 s, 20 s, 2 min, and 10 min). All perovskite films

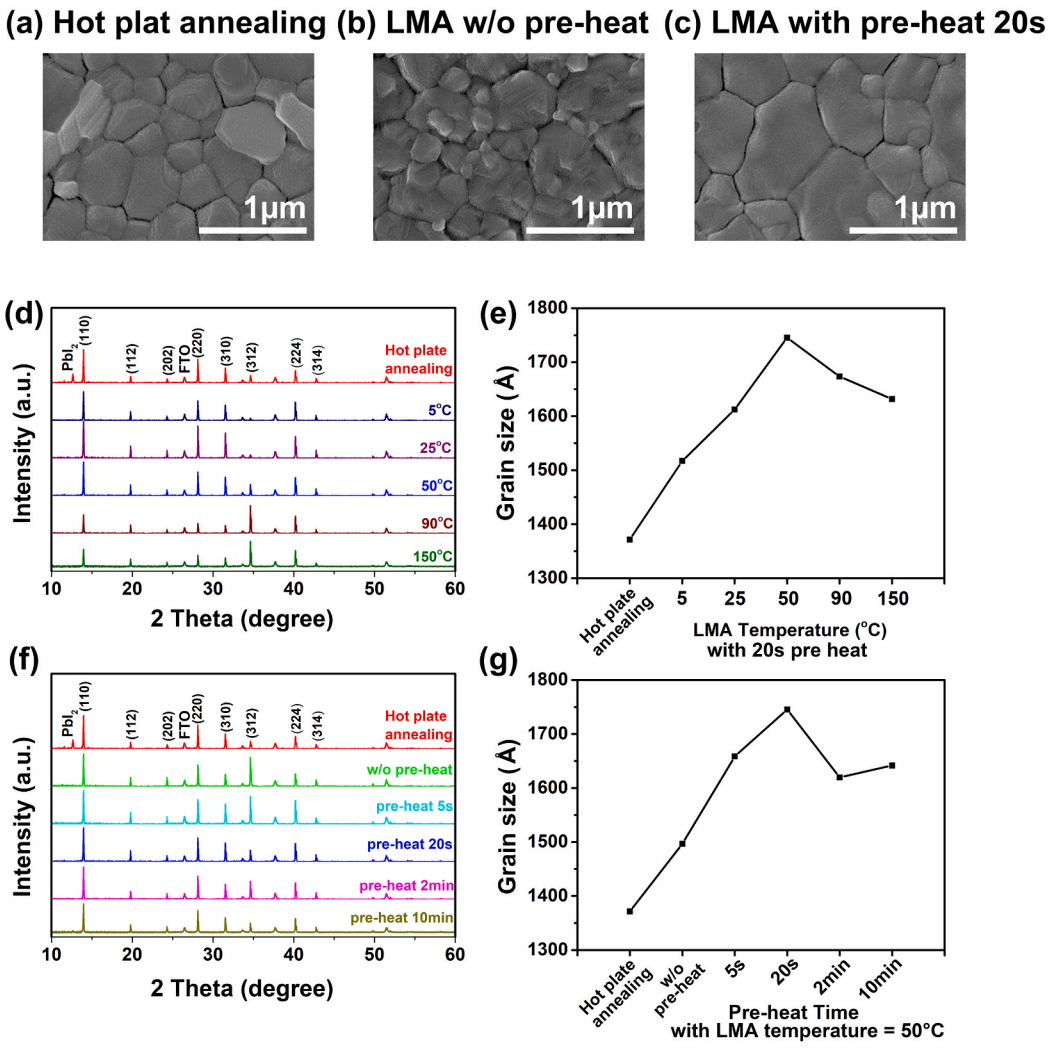

Fig. 1. Morphological and structural characterization of perovskite films produced under various annealing conditions. (a–c) Top-view scanning electron microscopy images of perovskite films prepared through (a) HPA, (b) LMA at 50 °C without preheating, and (c) LMA at 50 °C with 20 s of preheating at 135 °C. The scale bar in each image represents 1 μm. (d, f) Comparison of the X-ray diffraction (XRD) pattern of a perovskite film produced through HPA with those of perovskite films produced (d) through LMA at 5, 25, 50, 90, and 150 °C with 20-s preheating at 135 °C and (f) through LMA at 50 °C with preheating at 135 °C for 0 s, 5 s, 20 s, 2 min, and 10 min. (e, g) Variations in the average grain size of perovskite films with the (e) LMA temperature and (g) preheating time. The plots in (e) and (g) were derived from the XRD data in (d) and (f), respectively.

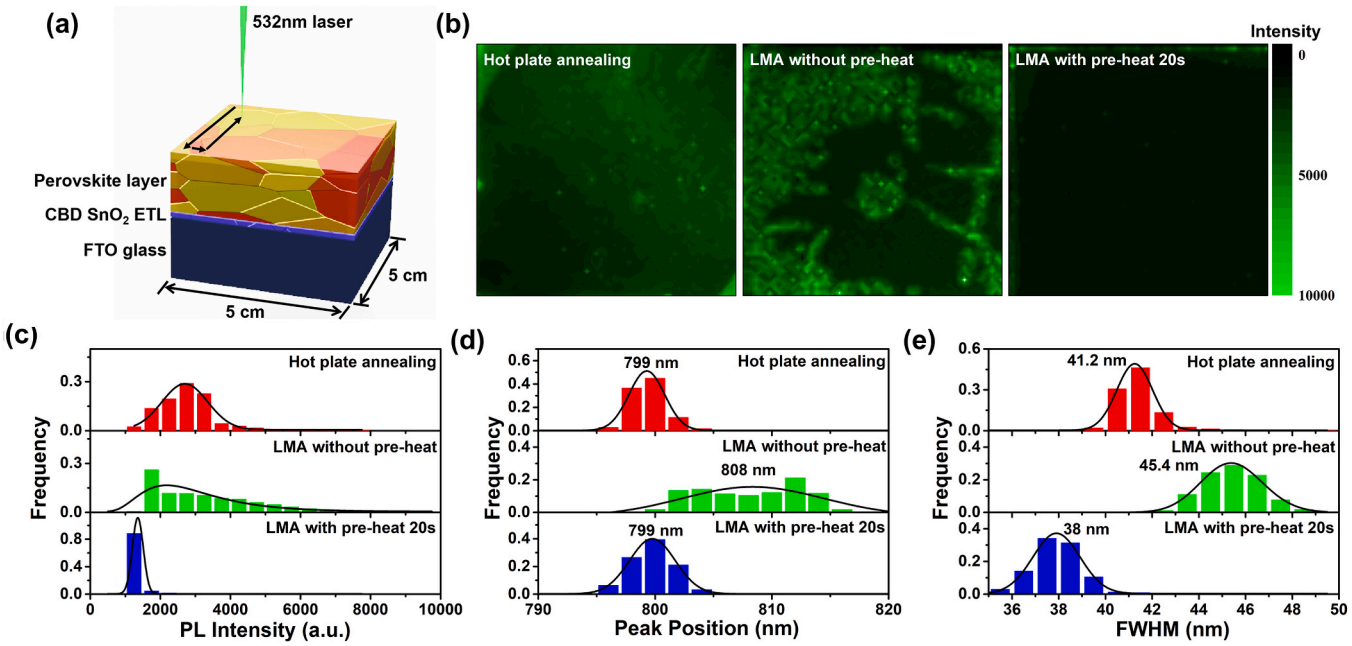

Fig. 2. (a) Schematic of PL mapping; (b) PL intensity maps of perovskite films prepared through HPA and through LMA at 50 °C with and without preheating for 20 s at 135 °C; and plots of (c) PL intensity, (d) PL peak position, and (e) full width at half-maximum values for these films.

produced through LMA exhibited characteristic diffraction peaks corresponding to the desired perovskite phase. The perovskite film produced through HPA exhibited a distinct PbI_2 peak at approximately 12.7°, which corresponds to the (001) plane of hexagonal PbI_2 [30,31], however, this peak was not exhibited by the films produced through LMA. The presence of a detectable PbI_2 peak often indicates incomplete conversion of precursors or the presence of excess PbI_2. Although a small quantity of excess PbI_2 can potentially enhance initial device

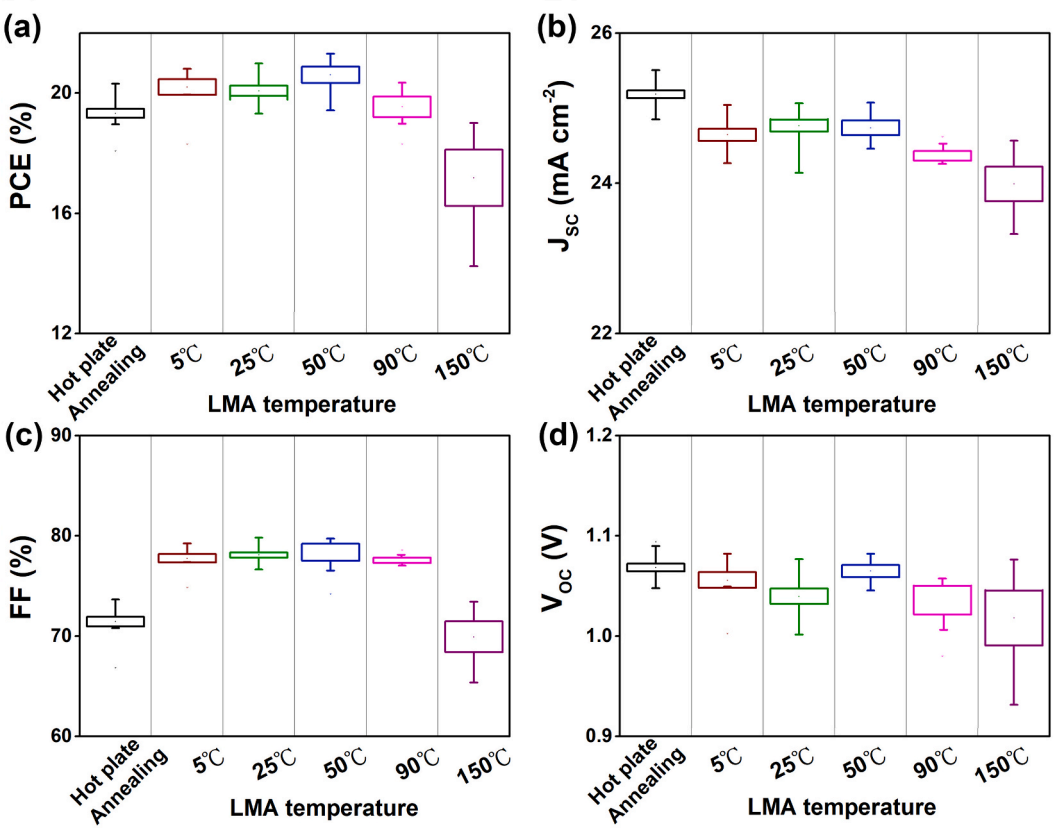

Fig. 3. Performance results of 30 PSCs produced through HPA and through LMA at different temperatures (5, 25, 50, 90, and 150 °C) with preheating at 20 s for 135 °C.

performance by improving film formation and passivating defects, its photolysis over time can lead to the formation of voids and trap states, which degrade device efficiency and long-term device stability [24]. Therefore, the effective minimization or elimination of residual PbI_2 in all perovskite films produced through LMA indicates that they had higher purity and potentially offered higher device stability than did that produced through HPA. As indicated in Fig. 1(e), the average grain size of the perovskite film increased with the LMA temperature up to 50 °C, which indicates that moderate-temperature annealing enhanced grain growth and improved crystallinity. The trend aligns with the general understanding that elevated annealing temperatures facilitate grain coalescence by increasing atomic mobility [32]. The largest grain size was achieved through LMA at 50 °C, and the corresponding film exhibited the highest photovoltaic performance among all fabricated films (Fig. 3). This annealing temperature was also employed in the study of Bücheler et al. [30]. In another study, increasing the LMA temperature to 90 and 150 °C slightly reduced the grain size, suggesting that excessive temperature may favor nucleation over growth, leading to more grain boundaries and defects [33]. Moreover, structural and interfacial degradation may occur at elevated temperatures, further compromising film quality [34]. The film prepared through LMA without preheating exhibited a markedly smaller grain size than did those prepared through LMA with preheating [Fig. 1(g)]. Notably, even a 5-s preheating process resulted in a substantial increase in grain size, indicating that preheating is essential for promoting effective crystal growth. This trend corresponds well with the PSC performance results displayed in Fig. 4. Overall, the SEM and XRD results highlight the critical roles of an appropriate LMA temperature and preheating in achieving uniform grain growth and high film quality.

To gain deeper insights into the causes underlying the divergent performance of the fabricated devices, the optoelectronic homogeneity and crystalline quality of the prepared perovskite films were comprehensively investigated through spatially resolved PL mapping. As illustrated in Fig. 2(a), a 532-nm laser was used to scan a 5 × 5 cm^2 area of each prepared film. The PL intensity maps in Fig. 2(b) reveal notable differences in the uniformity of the films produced through different approaches. The perovskite film prepared through HPA exhibited relatively uniform PL emission, whereas that produced through LMA without preheating exhibited considerably inhomogeneous PL emission, which was attributable to dried antisolvent droplets. Thus, incomplete antisolvent removal was the primary cause of the poor quality of the film produced through LMA without preheating. By contrast, the perovskite film produced through LMA with preheating for 20 s at 135 °C exhibited highly uniform PL emission and considerably suppressed PL intensity. These results are in agreement with the histograms depicted in Fig. 2(c), which suggest that the aforementioned film exhibited the lowest average PL intensity (1360 a.u.) and narrowest PL distribution among the prepared films. The film prepared through HPA had the highest average PL intensity (2700 a.u.). The excellent PL quenching in the film produced through LMA with preheating was a strong indicator of highly efficient charge carrier extraction at the interface between the perovskite layer and the electron transport layer (ETL) interface as well as a suppression of nonradiative recombination pathways. The histogram of PL peak position indicated that the electronic band structures of the films fabricated through HPA and through LMA with preheating were centered at 799 nm [Fig. S1(a)]. This result confirmed the formation of the desired perovskite phase with the expected optical properties in the aforementioned films and aligned with those of a previous study [31]. Conversely, the film that was prepared through LMA without preheating exhibited a broad and redshifted peak distribution centered at 808 nm, which was indicative of substantial variations in film composition, crystallinity, and internal strain [35]. In addition, among all films, that prepared through LMA with preheating exhibited the narrowest full width at half-maximum (FWHM) of the PL peak [Fig. 2(e)], indicating its high crystallinity, uniform grain size distribution, and low defect density [36]. The FWHM value of the aforementioned film (38 nm) was notably

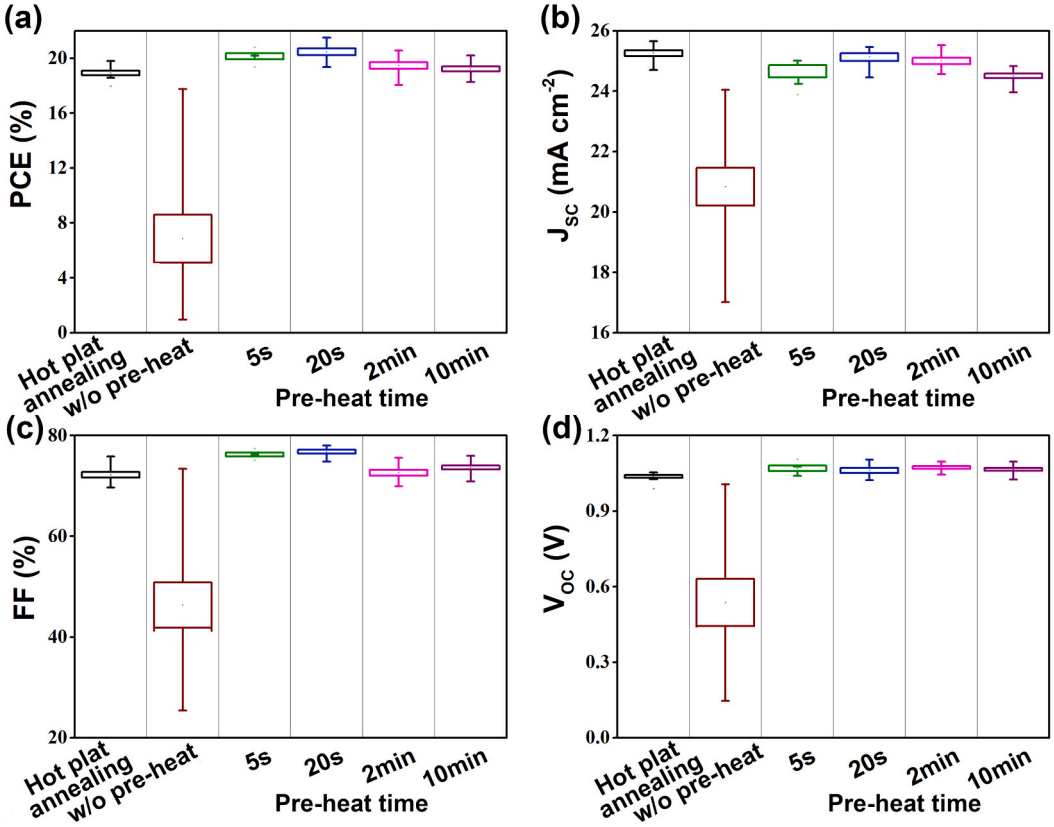

Fig. 4. Performance results of 30 PSCs fabricated through HPA and through LMA with preheating at 135 °C for various durations.

smaller than those of the films prepared through HPA (41.2 nm) and through LMA without preheating (45.4 nm). In summary, the PL mapping results suggest that incorporating a preheating step into LMA is crucial for eliminating residual antisolvent, thereby enabling the formation of perovskite films with excellent optoelectronic and crystalline quality.

The properties of PSCs containing a perovskite film prepared through LMA exhibited strong temperature dependence (Fig. 3). At a moderate temperature of 50 °C, the PCE and fill factor (FF) reached their highest values, likely because of the high crystallinity, low charge transport resistance, and minimal nonradiative recombination at this temperature. The temperature enabled the formation of high-quality perovskite films with limited defects and optimized carrier mobility. However, at 150 °C, the PCE and FF declined sharply, indicating that excessive thermal exposure introduces defects and structural degradation, which hinder charge extraction and increase resistance. A similar trend was observed for the short-circuit current density (J_{SC}), which had a high value at lower temperatures and then peaked at a moderate temperature of 50 °C, corresponding to intense carrier generation and efficient charge extraction. Previous studies have suggested that annealing temperatures exceeding 130 °C for 30 min can generate nonradiative defects, contributing to a reduction in FF and photovoltage [37]. In contrast, our results demonstrate that a lower, moderate temperature of 50 °C not only achieves superior PCE in PSCs but also significantly reduces the overall energy consumption during the fabrication process.

The effect of preheating duration on device performance was examined for PSCs with a perovskite film prepared under the optimal LMA and preheating temperatures of 50 and 135 °C, respectively (Fig. 4). When preheating was not conducted, the fabricated PSCs exhibited wide variations in the PCE, J_{SC} value, FF, and open-circuit voltage (V_{oc}), suggesting nonuniform film formation and inefficient charge extraction. Preheating for 20 s produced a uniform perovskite morphology comparable to that achieved through HPA, thus substantially improving the PSC performance. The alignment of the trends in Figs. 3 and 4 highlights the necessity of preheating to eliminate residual antisolvent and promote homogenous film crystallization. The aforementioned results also agree with the PL mapping results, which suggest that LMA with 20-s preheating produced a highly uniform film with low PL intensity (1360 a.u.) and high quenching efficiency, indicating efficient carrier extraction and reduced recombination. By contrast, the perovskite film produced through LMA without preheating exhibited broad PL intensity variations, highlighting the detrimental effect of incomplete solvent removal on film quality. Extensive research has highlighted that the annealing strategy reduces bond formation and crystallization rates. This strategy enables precise control of the annealing temperature and time, thus enabling the fabrication of uniform and dense thin films with limited defects [37,38].

On the basis of the aforementioned results, the optimal LMA time of 3mins, LMA temperature, preheating temperature, and preheating time were determined to be 3 min, 50 °C, 135 °C, and 20 s, respectively. A perovskite film was prepared through LMA with preheating under the aforementioned optimal conditions to fabricate a champion PSC, the photovoltaic performance of which was evaluated. Under reverse-scan (RS) conditions, this champion device exhibited a maximum PCE of 21.49%, a V_{oc} value of 1.104 V, a J_{SC} value of 24.96 mA/cm^2, and an FF of 77.81%. Moreover, under forward-scan (FS) conditions, it exhibited a PCE of 19.92%, a V_{oc} value of 1.09 V, a J_{SC} value of 24.71 mA/cm^2, and an FF of 73.81% in Table 1. Thus, the aforementioned device exhibited a hysteresis index (HI) of 0.073 [HI = ($PCE_{RS} - PCE_{FS}$)/PCE_{RS}], indicating its high stability and efficiency. FABr passivation is an effective strategy for addressing the persistent challenge of hysteresis in PSCs. This strategy leverages intermediate engineering and promotes the formation of active layers with large grain sizes and minimal defects, which are pivotal for enhancing device integrity and performance [39]. Therefore, the present study fabricated a perovskite film through LMA with preheating under the optimized conditions and then treated it with FABr to passivate its defects. This film was subsequently used to develop a PSC for comparison with the aforementioned champion PSC. Under FS and RS conditions, the PSC treated with FABr exhibited higher PCE (21.63% and 22.01%, respectively) and V_{oc} values (1.111 and 1.122 V, respectively) than did the PSC not treated with FABr. Moreover, the PSC treated with FABr exhibited a lower HI value (0.017). These substantial improvements [Fig. 5(b)] underscore the critical role of FABr passivation in mitigating hysteresis effects and enhancing the V_{oc} and FF values of PSCs. The deviations between the photocurrents of the two aforementioned PSCs were examined by analyzing their external quantum efficiency (EQE) spectra [Fig. 5(c)]. The device treated with FABr exhibited a strong and wide-range response within the spectral window of 300–850 nm, outperforming the device that was not treated with FABr in terms of photon-to-electron conversion efficiency across the majority of this spectral range. This result aligns with the trends observed in the current density–voltage (*J*–*V*) curves, which indicate that the integrated J_{SC} values of the PSCs treated and not treated with FABr were 24.28 and 23.46 mA/cm^2, respectively; thus, FABr passivation enhanced device performance. In addition, the EQE edge in Fig. S2 suggests that the bandgap of the PSC treated with FABr exhibited a blueshift, which is consistent with the absorption spectra obtained under different FABr concentrations [40,41].

Table 1
Photovoltaic parameters of the champion perovskite solar cells fabricated by LMA with pre-heat and the synergistic LMA + FABr passivation strategy.

Sample	Scan direction	V_{OC} (V)	J_{SC} (mA/cm^2)	FF (%)	PCE (%)
LMA with pre-heat 20 s	Forward	1.090	24.71	73.81	19.92
	Reverse	1.104	24.96	77.81	21.49
LMA with pre-heat 20 s +FABr passivation	Forward	1.111	25.31	76.53	21.63
	Reverse	1.122	25.30	77.13	22.01

To quantitatively characterize the defect properties of the aforementioned devices, we conducted measurements of space-charge-limited current (SCLC) for an electron-only device [FTO/SnO_2/PVSK/PCBM/Ag]. The SCLC results are presented in Fig. 6(b) and Table S3. The SCLC increased linearly with the voltage (corresponding to ohmic response) up to a transition point, following which it rose dramatically because of trap-state filling by injected carriers. After the trap state was completely filled, the SCLC exhibited a quadratic voltage dependence. The voltage at the transition point is defined as the trap-filled-limit voltage (V_{TFL}), which can be used to estimate the defect density [42]. The electron trap densities of the devices produced through HAP, LMA, and LMA + FABr passivation were estimated to be 5.21×10^{15}, 4.83×10^{15}, and 3.20×10^{15} cm^{-3}, respectively, demonstrating that defect formation was efficiently suppressed in the device produced through LMA and FABr passivation. A lower electron trap density is associated with higher perovskite film quality, leading to enhanced performance parameters for PSCs, including higher V_{oc} and FF values [23,43].

The steady-state PL and time-resolved PL (TRPL) spectra of the devices were obtained to assess the recombination reactions and carrier lifetime within their perovskite films [Figs. S4 and (c)]. The devices fabricated through LMA exhibited considerably higher steady-state PL intensities than did that fabricated through HPA, indicating that LMA substantially suppressed the nonradiative recombination caused by defects [44]. The devices produced through LMA had PL emission peaks at 801 and 791 nm, respectively, indicating that FABr passivation caused the blueshift of the emission peak. This blueshift was attributable to the reduced trap density and defect states on the interface between the perovskite film and HTL in the device fabricated through LMA and FABr passivation [45,46]. Removing traps near the band edge promotes higher-energy radiative recombination of excitons, resulting in a blue-shifted emission peak [47]. To elucidate the carrier recombination mechanisms of the three devices, their TRPL decay curves were analyzed. These curves were well-described by the biexponential decay

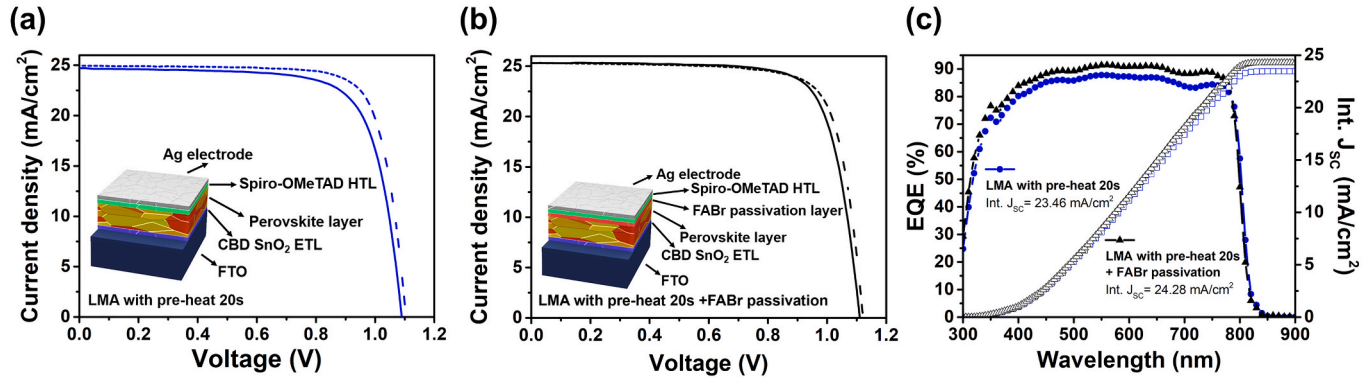

Fig. 5. Current density–voltage (*J*–*V*) plots of champion devices under simulated sunlight: (a) PSC with a perovskite film prepared through a process involving LMA and preheating at 135 °C for 20 s and (b) PSC with a perovskite film prepared through a process involving LMA, preheating at 135 °C for 20 s, and FABr passivation. (c) External quantum efficiency spectra (left axis) and corresponding integrated J_{SC} values (right axis) for the two champion PSCs.

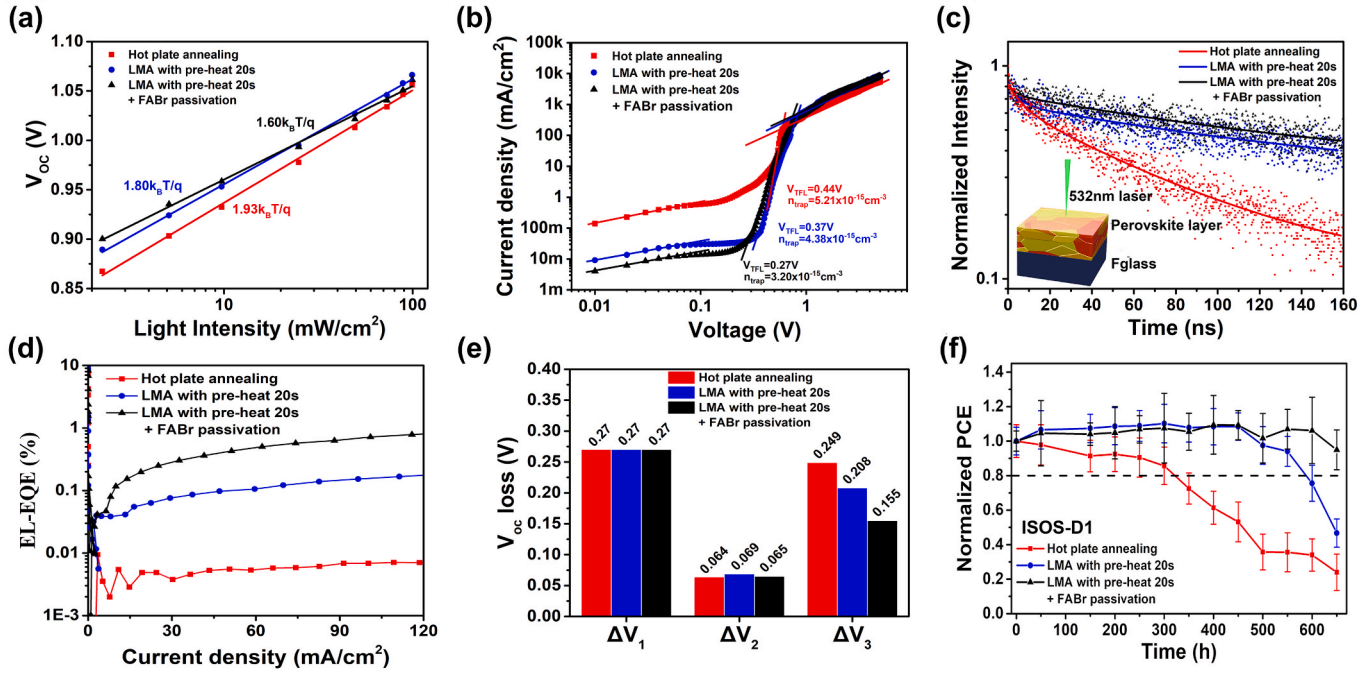

Fig. 6. Optoelectronic properties and stability of PSCs fabricated through HPA, through LMA with preheating for 20 s but without FABr passivation, and through LMA with preheating for 20 s and FABr passivation. (a) Variations in the open-circuit voltage (V_{oc}) with light intensity. (b) Measurements of the space-charge-limited current. (c) Measurements of the time-resolved PL. The inset depicts a schematic of the experimental setup. (d) EL-EQE values of the examined PSCs. (e) Radiative and nonradiative V_{oc} losses of the investigated PSCs. Variations in the normalized average PCEs of five unencapsulated PSCs with different conditions under the (f) ISOS-D1 protocol.

function $I(t) = A_1\, e^{-t/\tau_1} + A_2\, e^{-t/\tau_2}$ [48], where τ_1 and τ_2 represent the fast (trap-assisted nonradiative recombination) and slow (intrinsic radiative recombination in the bulk film) components, respectively. The average lifetime of carriers (τ_{avg}) was estimated using the formula $\tau_{avg} = (A_1\tau_1 + A_2\tau_2)/100$, where A_1 and A_2 are the amplitudes. Parameters related to the carrier lifetimes of the three devices are presented in Table S4. The PSC through LMA caused a dramatic increase in τ_2 (from 69.35 to 145.63 ns), confirming its primary role in improving bulk film quality. The short average carrier lifetime (τ_{avg} = 55.08 ns) of perovskite film through HPA is only half of that through LMA (τ_{avg} = 115.60 ns). On the other hand, the subsequent FABr passivation caused only a negligible improvement (145.63 to 145.99 ns). This means it did not further enhance the bulk structure. At the same time, FABr passivation reduces the amplitude (A1) of the fast decay component from 22% (LMA) to 17% (LMA and FABr passivation) This distinct reduction in A1 confirms that FABr passivation effectively shifts the dominant recombination pathway away from the fast channels to another slow channel, thus leading to the final improvement in τ_{avg}. By comparison, the τ_{avg} of the film fabricated using LMA and FABr passivation was 122.78 ns, by improving from 115.60 ns of perovskite film through LMA. This finding was verified by the SCLC measurements, which indicated that the devices produced using LMA and FABr passivation had considerably lower trap density than did those produced using HPA [49].

The V_{oc} losses of the three devices were analyzed in detail to assess performance [Fig. 6(e) and S5]. The total V_{oc} loss was deconvoluted into three components: ΔV_1, ΔV_2, and ΔV_3. The component ΔV_1 represents the fundamental radiative recombination loss related to the Shockley–Queisser limit. This component did not vary across the three devices, exhibiting a constant value of 0.270 V because the devices were constructed using the same perovskite material. The component ΔV_2 arises from sub-bandgap absorption that leads to black-body radiation. It was quantified through highly sensitive EQE measurements and

demonstrated negligible variation across the three devices (0.064–0.069 V). The aforementioned results suggest that ΔV_3 was the main component responsible for the differences among the V_{oc} values of the three devices. This component, which arises from nonradiative recombination, was calculated to be 0.249 V for the device produced through HPA. The device fabricated using LMA had a lower ΔV_3 value of 0.208 V. This decrease was caused by the enlarged perovskite grain size induced by LMA (as indicated by the XRD results), which decreased the number of defects at perovskite–perovskite interfaces. Furthermore, the device produced through LMA and FABr passivation had an even lower ΔV_3 value of 0.155 V, which was attributable to the mitigation of interfacial defects between the perovskite layer and the HTL [50]. These results indicate that method (LMA + 20-s preheating + FABr passivation) effectively mitigates nonradiative recombination, thereby minimizing voltage losses and maximizing the device's V_{oc} value.

Long-term operational stability is essential for the practical viability of PSCs. Therefore, in accordance with the ISOS-D1 protocol (temperature: 25 ± 5 °C, relative humidity: 50% ± 5%), this study rigorously evaluated the ambient stability of unencapsulated devices [51]. After 650 h of continuous exposure, the PSC produced through LMA and FABr passivation exhibited excellent durability, retaining 94.5% of its initial PCE. By contrast, the device fabricated using HPA exhibited severe performance degradation, with its PCE decreasing to 46.7% of the initial value. Notably, during the initial 500 h, both aforementioned PSCs exhibited substantially greater stability than the device fabricated through HPA did. This initial resilience was attributable to the LMA treatment enhancing the perovskite film's intrinsic quality and suppressing defect formation on the perovskite–perovskite interface, thereby enhancing the film's resistance to moisture ingress. However, the divergence in performance beyond 500 h underscores the critical role of interfacial engineering through FABr passivation. The aforementioned findings suggest that PSCs with robust long-term stability can be fabricated using a synergistic strategy that involves enhancing the quality of bulk perovskite films through LMA and then using FABr for interfacial passivation. On the other hand, the devices were also tested under white light soaking at room temperature in N_2 glovebox. In Fig. S6, we find that PCE degradation mainly stems from V_{OC} degradation. Defects in the perovskite film can evolve into non-radiative recombination centers under light illumination, leading to further degradation [52]. So the lower trap density of PSC through LMA (from SCLC and TRPL analysis) shows better light soaking performance. Finally, the PSC through LMA and FABr passivation keeps 86.2% of its initial PCE.

3. Conclusions

This study developed a synergistic strategy for enhancing the efficiency and stability of PSCs. This strategy involves LMA for 3 min at a moderate temperature of 50 °C, preheating at 135 °C for 20 s, and FABr passivation. The pre-heating treatment is indispensable for eliminating residual antisolvent and promoting homogeneous crystallization, facilitating the formation of continuous perovskite films with large grains, high crystallinity, and low defect density. A PSC prepared using the aforementioned strategy but without FABr passivation exhibited a champion PCE of 21.49% and suppressed hysteresis. Moreover, a PSC produced using the aforementioned strategy with FABr passivation had a higher PCE of 22.01%. This increase was related to FABr passivation effectively reducing interfacial trap density and extending carrier lifetime. An unencapsulated device fabricated using the proposed approach with FABr passivation retained 94.5% of its initial PCE after 650 h under ISOS-D1 testing, underscoring the importance of combining film quality improvement and interfacial passivation for long-term operational stability. In summary, the proposed approach offers a scalable and energy-efficient route for fabricating high-performance and durable PSCs. The results of this study can provide valuable guidance for the future commercialization of PSCs.

4. Experimental section

4.1. Materials

N,N-Dimethylaniline (99%) and Tin(II) chloride dihydrate ($SnCl_2{\cdot}2H_2O$, 99%) were purchased from Alfa Aesar. 4-*tert*-butylpyridine (4-tBP, 99.99%), cesium iodide (CsI, >99.99%), lithium bis(trifluoromethylsulphonyl)imide (LiTFSI, 99.9%), thioglycolic acid (TGA, 98%) were purchased from Sigma–Aldrich. Potassium carbonate (K_2CO_3, 99%) were purchased from ACROS. Formamidinium bromide (FABr, >99.99%), formamidinium iodide (FAI, >99.99%), methylammonium iodide (MAI, 98%) were purchased from FMPV. Urea was purchased from J.T.Baker. Spiro-OMeTAD was purchased from Ruilong. Dimethyl sulfoxide (DMSO, 99.9%) and dimethylformamide (DMF, 99.5%) were sourced from Echo Chemical Co., Ltd. Anisole (99%), ethyl benzoate (EB, >99%) were purchased from Thermo Scientific Chemicals.

4.2. Device fabrication

The detailed PSC fabrication procedure of the perovskite solar cells is illustrated in Fig. 7. Fluorine-doped tin oxide (FTO) glass substrates were sequentially cleaned using deionized (DI) water, acetone, ethanol, and isopropanol. To enhance the surface hydrophilicity, the cleaned substrates were subjected to UV ozone treatment for 40 min. Following surface cleaning, a SnO_2 electron transport layer (ETL) was deposited via a chemical bath deposition (CBD) method, as described in our previous work [53]. The precursor solution comprised 781.3 mg of urea, 781.3 μL of concentrated hydrochloric acid, 15.8 μL of thioglycolic acid, and 171.9 mg of tin(II) chloride dihydrate, all dissolved in 500 mL of DI water. The FTO substrates were placed horizontally in the CBD solution and maintained at 70 °C for 3 hr. Following ETL deposition, the substrates were rinsed 3–4 times with DI water, dried under a nitrogen stream, and subsequently annealed at 180 °C for 60 min on a hot plate. A ETL post-treatment step was then performed by spin-coating a sodium carbonate solution (27.6 mg Na_2CO_3 in 20 ml DI water) at 3000 rpm for 30 s, followed by drying at 105 °C for 10 mins. After weighing 13.0 mg of CsI, 31.8 mg of MAI, 129.0 mg of FAI, and 464.0 mg of PbI_2 powders in a glovebox, 800 μL of DMSO and 200 μL of DMF were added. The mixture was stirred at 45 °C for over 40 min to obtain the perovskite precursor solution with a composition of $FA_{0.75}MA_{0.2}Cs_{0.05}PbI_3$. The triple-cation perovskite layer was deposited via a two-step spin-coating process: initially at 1000 rpm for 10 s and then at 5000 rpm for 20 s. At the final 3 s, 100 μL of toluene as an anti-solvent was dynamically dispensed onto the center of the substrate. The films were then subjected to one of three annealing protocols: (i) hot plate annealing (HPA), (ii) liquid medium annealing (LMA) using anisole as the medium with 135 °C pre-heat, and (iii) LMA using anisole as the medium with pre-heating followed by FABr passivation. In this study, different pre-heat times and LMA temperatures were adjusted to investigate the physical mechanisms in PSCs. For devices with FABr passivation, 75 μL of a 0.25 mg/mL FABr solution in isopropanol (IPA) was spin-coated at 3000 rpm for 30 s on LMA perovskite film with 135 °C 20 s pre-heat. The films were then dried on a hot plate at 100 °C for 10 min to remove residual solvent. Subsequently, the hole transport layer (HTL) was deposited by spin-coating 75 μL of Spiro-OMeTAD solution at 2000 rpm for 30 s. The Spiro-OMeTAD solution was prepared in chlorobenzene at a concentration of 40 mg/mL, with additives including 17.5 μL of lithium bis(trifluoromethanesulfonyl)imide (Li-TFSI; 520 mg/mL in acetonitrile) and 28.5 μL of 4-*tert*-butylpyridine. Finally, a 100 nm thick silver (Ag) electrode with an active area of 0.09 cm^2 was thermally evaporated at a deposition rate of 1 Å/s, thereby completing the fabrication of the n-i-p structured perovskite solar cell.

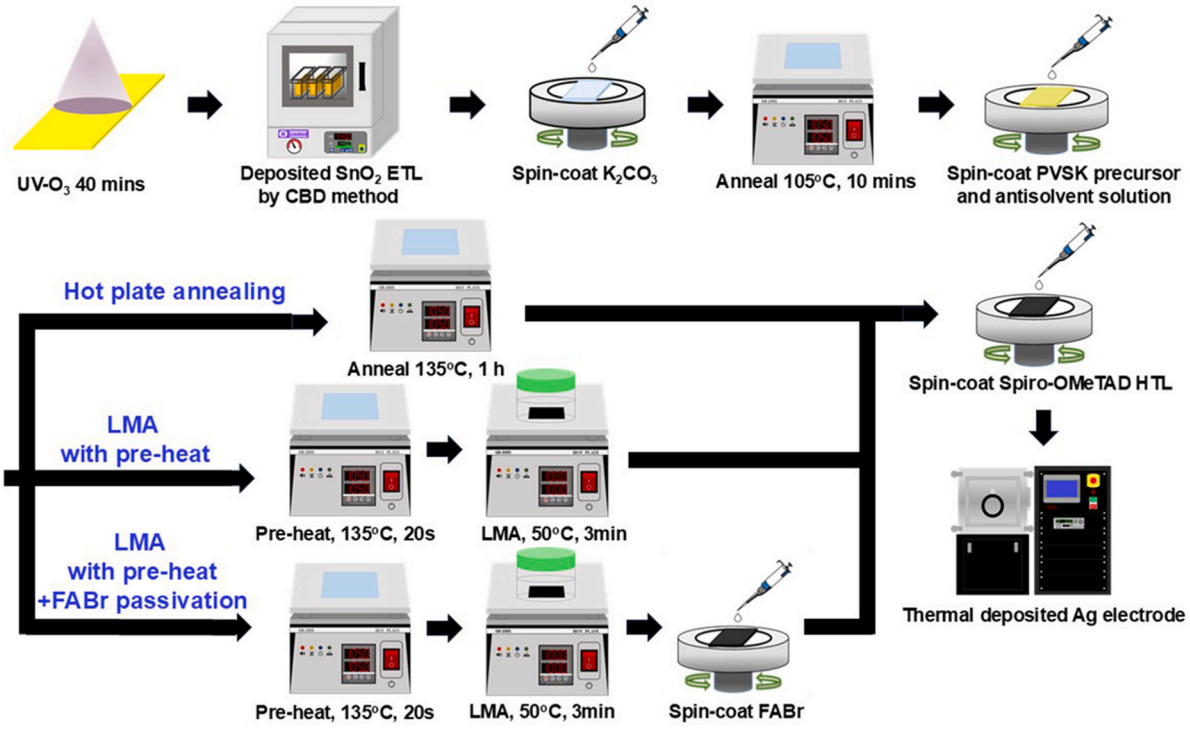

Fig. 7. Flowchart of the PSC fabrication process.

4.3. Characterization

The photovoltaic performance of the fabricated devices was characterized by current density–voltage (J-V) measurements using a digital source meter (Keithley 2400) under simulated AM 1.5G solar illumination (100 mW cm^{-2}), calibrated with a Si-reference cell (BS-520BK, Bunkokeiki) equipped with a KG-5 filter. The J-V scans were performed in both forward (−0.1 to 1.2 V) and reverse (1.2 to −0.1 V) directions with a voltage step of 10 mV and a delay time of 50 ms. External quantum efficiency (EQE) spectra were recorded using an EQE spectrometer (EQE-R-3011, Enli Technology Co. Ltd). The surface morphology of each film was examined through field-emission SEM (SU-8010, HITACHI), whereas the crystal structures of the films were analyzed through XRD analysis (D8 Focus, Bruker). Moreover, steady-state PL and TRPL spectra were collected using a 532-nm diode laser (LDH-D-TA-530, PicoQuant), with TRPL signals acquired using a time-correlated single-photon counting system (TimeHarp 260, PicoQuant). The open-circuit voltage loss (V_{oc} loss) was evaluated using a V_{oc} loss analysis system (REPS, Enli Technology Co. Ltd.). Finally, optical bandgaps were estimated from Tauc plots obtained through UV–vis spectroscopy (V-730, Jasco).

Declaration of Generative AI and AI-assisted technologies in the writing process

During the preparation of this work, the authors used ChatGPT (GPT-3.5) solely to improve the language and readability of the manuscript, as permitted by the publisher's policy. The AI tool was not used to generate images or analyze data. The authors have thoroughly reviewed and edited the content and take full responsibility for the article

CRediT authorship contribution statement

Wei-Hao Chiu: Writing – original draft, Data curation. **Wei-Lun Yu:** Formal analysis, Data curation. **Ming-Chung Wu:** Writing – review & editing. **Jen-Fu Hsu:** Writing – review & editing. **Gao Chen:** Writing – review & editing. **Ching-Yuan Liu:** Writing – review & editing. **Kun-Mu Lee:** Writing – review & editing, Supervision, Investigation.

Declaration of competing interest

The authors declare that they have no known competing financial interests or personal relationships that could have appeared to influence the work reported in this paper.

Acknowledgments

The authors thank the support from National Science and Technology Council, Taiwan (Grant Number NSTC 111-2113-M-008-008 and NSTC 108-2628-E-182-003-MY4), Chang Gung University (URRPD2Q0011) and Chang Gung Memorial Hospital, Linkou, Taiwan (CMRPD2L072).

Appendix A. Supplementary data

Supplementary data to this article can be found online at https://doi.org/10.1016/j.solener.2026.114430.

Data availability

The authors do not have permission to share data.

References

[1] A. Al-Ashouri, E. Köhnen, B. Li, A. Magomedov, H. Hempel, P. Caprioglio, J. A. Márquez, A.B. Morales Vilches, E. Kasparavicius, J.A. Smith, N. Phung, D. Menzel, M. Grischek, L. Kegelmann, D. Skroblin, C. Gollwitzer, T. Malinauskas, M. Jošt, G. Matič, B. Rech, R. Schlatmann, M. Topič, L. Korte, A. Abate, B. Stannowski, D. Neher, M. Stolterfoht, T. Unold, V. Getautis, S. Albrecht, Monolithic perovskite/silicon tandem solar cell with 29% efficiency by enhanced hole extraction, Science 370 (2020) 1300–1309.
[2] M.M. Lee, J. Teuscher, T. Miyasaka, T.N. Murakami, H.J. Snaith, Efficient hybrid solar cells based on meso-superstructured organometal halide perovskites, Science 338 (2012) 643–647.

[3] M. Saliba, T. Matsui, J.-Y. Seo, K. Domanski, J.-P. Correa-Baena, M.K. Nazeeruddin, S.M. Zakeeruddin, W. Tress, A. Abate, A. Hagfeldt, Cesium-containing triple cation perovskite solar cells: improved stability, reproducibility and high efficiency, Energ. Environ. Sci. 9 (2016) 1989–1997.
[4] T. Zhou, M. Wang, Z. Zang, X. Tang, L. Fang, Two-dimensional lead-free hybrid halide perovskite using superatom anions with tunable electronic properties, Sol. Energy Mater. Sol. Cells 191 (2019) 33–38.
[5] A. Kojima, K. Teshima, Y. Shirai, T. Miyasaka, Organometal halide perovskites as visible-light sensitizers for photovoltaic cells, J. Am. Chem. Soc. 131 (2009) 6050–6051.
[6] S. Bhattarai, M.K. Hossain, R. Pandey, J. Madan, D.P. Samajdar, M.F. Rahman, M. Z. Ansari, M. Amami, Perovskite solar cells with dual light absorber layers for performance efficiency exceeding 30%, Energy Fuel 37 (2023) 10631–10641.
[7] Q. Zhang, H. Huang, Y. Yang, M. Wang, S. Qu, Z. Lan, T. Jiang, Z. Wang, S. Du, Y. Lu, Y. Suo, P. Cui, M. Li, A universal ternary solvent system of surface passivator enables perovskite solar cells with efficiency exceeding 26%, Adv. Mater. 36 (2024) 2410390.
[8] Y. Zheng, Y. Li, R. Zhuang, X. Wu, C. Tian, A. Sun, C. Chen, Y. Guo, Y. Hua, K. Meng, Towards 26% efficiency in inverted perovskite solar cells via interfacial flipped band bending and suppressed deep-level traps, Energ. Environ. Sci. 17 (2024) 1153–1162.
[9] C. Liu, Y.-B. Cheng, Z. Ge, Understanding of perovskite crystal growth and film formation in scalable deposition processes, Chem. Soc. Rev. 49 (2020) 1653–1687.
[10] G. Kim, C.S. Moon, T.-Y. Yang, Y.Y. Kim, J. Chung, E.H. Jung, T.J. Shin, N.J. Jeon, H.H. Park, J. Seo, A thermally induced perovskite crystal control strategy for efficient and photostable wide-bandgap perovskite solar cells, Sol. RRL 4 (2020) 2000033.
[11] A.H. Ghahremani, D. Ratnayake, A. Sherehiy, D.O. Popa, T. Druffel, Automated fabrication of perovskite photovoltaics using inkjet printing and intense pulse light annealing, Energ. Technol. 9 (2021) 2100452.
[12] G. Yu, K.-J. Jiang, W.-M. Gu, Y. Li, Y. Lin, Y. Xu, X. Jiao, T. Xue, Y. Zhang, Y. Song, Vacuum-assisted thermal annealing of CsPbI3 for highly stable and efficient inorganic perovskite solar cells, Angew. Chem. Int. Ed. 61 (2022) e202203778.
[13] C. Ge, Q. Xu, D. Liu, W. Ye, Y. Zhu, P. Zhang, J. Yang, G. Liang, L. Xu, Y. Zhou, Light radiation annealing enables unidirectional crystallization of vacuum-assisted Sn–Pb perovskites for efficient tandem solar cells, Energ. Environ. Sci. 18 (2025) 430–438.
[14] J. Jiang, W. Tang, X. Yang, X. Sun, J. Yang, H.L. Cai, F.M. Zhang, X.S. Wu, Improvement of quality and stability of MAPbI3 films grown by post annealing under high pressure argon atmosphere, J. Phys. D Appl. Phys. 54 (2021) 075101.
[15] N. Li, X. Niu, L. Li, H. Wang, Z. Huang, Y. Zhang, Y. Chen, X. Zhang, C. Zhu, H. Zai, Y. Bai, S. Ma, H. Liu, X. Liu, Z. Guo, G. Liu, R. Fan, H. Chen, J. Wang, Y. Lun, X. Wang, J. Hong, H. Xie, D.S. Jakob, X.G. Xu, Q. Chen, H. Zhou, Liquid medium annealing for fabricating durable perovskite solar cells with improved reproducibility, Science 373 (2021) 561–567.
[16] Q. Jiang, Y. Zhao, X. Zhang, X. Yang, Y. Chen, Z. Chu, Q. Ye, X. Li, Z. Yin, J. You, Surface passivation of perovskite film for efficient solar cells, Nat. Photonics 13 (2019) 460–466.
[17] S. Teale, M. Degani, B. Chen, E.H. Sargent, G. Grancini, Molecular cation and low-dimensional perovskite surface passivation in perovskite solar cells, Nat. Energy 9 (2024) 779–792.
[18] J. Zhuang, P. Mao, Y. Luan, X. Yi, Z. Tu, Y. Zhang, Y. Yi, Y. Wei, N. Chen, T. Lin, F. Wang, C. Li, J. Wang, Interfacial passivation for perovskite solar cells: the effects of the functional group in phenethylammonium iodide, ACS Energy Lett. 4 (2019) 2913–2921.
[19] F. Zhang, Q. Huang, J. Song, Y. Zhang, C. Ding, F. Liu, D. Liu, X. Li, H. Yasuda, K. Yoshida, J. Qu, S. Hayase, T. Toyoda, T. Minemoto, Q. Shen, Growth of amorphous passivation layer using phenethylammonium iodide for high-performance inverted perovskite solar cells, Sol. RRL 4 (2020) 1900243.
[20] Q. Cheng, H. Xia, X. Li, B. Wang, Y. Li, X. Zhang, H. Zhang, Y. Zhang, H. Zhou, High-efficiency and stable perovskite solar cells enabled by low-dimensional perovskite surface modifiers, Sol. RRL 6 (2022) 2100805.
[21] W. Liu, W. Sun, K. Wang, H. Xu, X. Huo, R. Yin, Y. Sun, S. Ji, T. You, W. Li, P. Yin, Surface passivation of CsPbI 3 films for efficient and stable hole-transporting layer-free carbon-based perovskite solar cells, ACS Appl. Energy Mater. 6 (2023) 3495–3503.
[22] O. Hakami, J.F. Rasheed, T. Zelai, F. Khan, A.S. Alshomrany, F. Khan, Investigation of FABr treatment's potential for triple-cation multi-halide perovskite solar cells, Sol. Energy 274 (2024) 112590.
[23] J. Suo, B. Yang, E. Mosconi, H.-S. Choi, Y. Kim, S.M. Zakeeruddin, F. De Angelis, M. Grätzel, H.-S. Kim, A. Hagfeldt, Surface reconstruction engineering with synergistic effect of mixed-salt passivation treatment toward efficient and stable perovskite solar cells, Adv. Funct. Mater. 31 (2021) 2102902.
[24] Q. Zou, G. Zheng, D. Yao, J. Wang, N. Tian, S. Mo, F. Long, Effects of lead iodide crystallization on photovoltaic performance of perovskite solar cells by the vapor-solid reaction method, ACS Omega 8 (2023) 12430–12438.
[25] X. Zhang, J. Huang, H. Zuo, Y. Zhang, R. Yang, J. Chen, G. Li, W. Li, Z. Peng, Surface planarization enabled low-dimensional perovskite-leveling compound for carbon-based CsPbI2Br perovskite solar cells, Sol. Energy Mater. Sol. Cells 292 (2025) 113798.
[26] R.K. Koech, Y.A. Olanrewaju, R. Ichwani, M. Kigozi, D.O. Oyewole, O.V. Oyelade, D.M. Sanni, S.A. Adeniji, E. Colin-Ulloa, L.V. Titova, J.L. Martin, R.L. Grimm, A. Bello, O.K. Oyewole, E. Ntsoenzok, W.O. Soboyejo, Effects of polyethylene oxide particles on the photo-physical properties and stability of FA-rich perovskite solar cells, Sci. Rep. 12 (2022) 12860.
[27] W. Li, J. Fan, J. Li, Y. Mai, L. Wang, Controllable grain morphology of perovskite absorber film by molecular self-assembly toward efficient solar cell exceeding 17%, J. Am. Chem. Soc. 137 (2015) 10399–10405.
[28] F. Wang, S. Bai, W. Tress, A. Hagfeldt, F. Gao, Defects engineering for high-performance perovskite solar cells, npj Flexible Electron. 2 (2018) 22.
[29] W.S. Yang, J.H. Noh, N.J. Jeon, Y.C. Kim, S. Ryu, J. Seo, S.I. Seok, High-performance photovoltaic perovskite layers fabricated through intramolecular exchange, Science 348 (2015) 1234–1237.
[30] F. Fu, T. Feurer, T. Jäger, E. Avancini, B. Bissig, S. Yoon, S. Buecheler, A.N. Tiwari, Low-temperature-processed efficient semi-transparent planar perovskite solar cells for bifacial and tandem applications, Nat. Commun. 6 (2015) 8932.
[31] S. Ahn, W.-H. Chiu, H.-M. Cheng, V. Suryanarayanan, G. Chen, Y.-C. Huang, M.-C. Wu, K.-M. Lee, Enhancing efficiency and stability of perovskite solar cells through two-step deposition method with the addition of cesium halides to PbI2 precursor, Org. Electron. 120 (2023) 106847.
[32] S. Abbasi, X. Wang, P. Tipparak, C. Bhoomanee, P. Ruankham, H. Liu, D. Wongratanaphisan, W. Shen, Proper annealing process for a cost effective and superhydrophobic ambient-atmosphere fabricated perovskite solar cell, Mater. Sci. Semicond. Process. 155 (2023) 107241.
[33] J.J. Jerónimo-Rendon, S. Gholipour, S. Svetlosanova, R. Roy, S. Boehringer, S. Topcu, W. Zuo, M. Zohdi, M. Ataei, M. Kedia, A. Zhuravlova, S.-H. Turren-Cruz, P. Samorì, A.G. Ricciardulli, M. Malekshahi Byranvand, M. Saliba, High coordination-solvent bathing for efficient crystallization of MA-free triple halide perovskite solar cells, EES Solar 1 (2025) 30–40.
[34] D.R. Wargulski, K. Xu, H. Hempel, M.A. Flatken, S. Albrecht, D. Abou-Ras, Relationship between the annealing temperature and the presence of PbI2 platelets at the surfaces of slot-die-coated triple-halide perovskite thin films, ACS Appl. Mater. Interfaces 15 (2023) 41516–41524.
[35] C. Zhu, X. Niu, Y. Fu, N. Li, C. Hu, Y. Chen, X. He, G. Na, P. Liu, H. Zai, Y. Ge, Y. Lu, X. Ke, Y. Bai, S. Yang, P. Chen, Y. Li, M. Sui, L. Zhang, H. Zhou, Q. Chen, Strain engineering in perovskite solar cells and its impacts on carrier dynamics, Nat. Commun. 10 (2019) 815.
[36] S. Du, Y. Guo, C. Wang, G. Chen, G. Li, J. Liang, W. Chen, Z. Yu, Y. Ge, P. Jia, H. Guan, Z. Yu, H. Cui, Z. Yu, W. Ke, G. Fang, Improving crystallization of wide-bandgap lead halide perovskite for all-perovskite tandems, Adv. Energy Mater. 15 (2025) 2404180.
[37] X. Gu, C. Shan, X. Xu, Q. Liu, A.K.K. Kyaw, Antisolvent-free heterogenous nucleation enabled by employing 4-tert-butyl pyridine additive and two-step annealing for efficient CsPbI2Br perovskite solar cells, Small 20 (2024) 2307840.
[38] J. Zhang, W. Liang, W. Yu, S. Yu, Y. Wu, X. Guo, S. Liu, C. Li, A two-stage annealing strategy for crystallization control of CH3NH3PbI3 films toward highly reproducible perovskite solar cells, Small 14 (2018) 1800181.
[39] M. Mateen, Z. Arain, X. Liu, C. Liu, Y. Yang, Y. Ding, S. Ma, Y. Ren, Y. Wu, Y. Tao, P. Shi, S. Dai, High-performance mixed-cation mixed-halide perovskite solar cells enabled by a facile intermediate engineering technique, J. Power Sources 448 (2020) 227386.
[40] Y. Haruta, H. Ye, P. Huber, N. Sandor, A. Pavesic Junior, S. Dayneko, S. Qiu, V. Yeddu, M.I. Saidaminov, Reproducible high-quality perovskite single crystals by flux-regulated crystallization with a feedback loop, Nat. Synth. 3 (2024) 1212–1220.
[41] K.T. Cho, S. Paek, G. Grancini, C. Roldán-Carmona, P. Gao, Y. Lee, M. K. Nazeeruddin, Highly efficient perovskite solar cells with a compositionally engineered perovskite/hole transporting material interface, Energ. Environ. Sci. 10 (2017) 621–627.
[42] J. Peng, Y. Chen, K. Zheng, T. Pullerits, Z. Liang, Insights into charge carrier dynamics in organo-metal halide perovskites: from neat films to solar cells, Chem. Soc. Rev. 46 (2017) 5714–5729.
[43] V.M. Le Corre, E.A. Duijnstee, O. El Tambouli, J.M. Ball, H.J. Snaith, J. Lim, L.J. A. Koster, Revealing charge carrier mobility and defect densities in metal halide perovskites via space-charge-limited current measurements, ACS Energy Lett. 6 (2021) 1087–1094.
[44] H. Cho, S.-H. Jeong, M.-H. Park, Y.-H. Kim, C. Wolf, C.-L. Lee, J.H. Heo, A. Sadhanala, N. Myoung, S. Yoo, S.H. Im, R.H. Friend, T.-W. Lee, Overcoming the electroluminescence efficiency limitations of perovskite light-emitting diodes, Science 350 (2015) 1222–1225.
[45] L. Zhu, S. Xu, G. Liu, L. Liu, H. Zhou, Z. Ai, X. Pan, F. Zhang, Engineering the passivation routes of perovskite films towards high performance solar cells, Chem. Sci. 15 (2024) 5642–5652.
[46] L. Zhang, G. Luo, W. Zhang, Y. Yao, P. Ren, X. Geng, Y. Zhang, X. Wu, L. Xu, P. Lin, Strain regulation and defect passivation of FA-based perovskite materials for highly efficient solar cells, Adv. Sci. 11 (2024) 2305582.
[47] M. Salado, A.D. Jodlowski, C. Roldan-Carmona, G. de Miguel, S. Kazim, M. K. Nazeeruddin, S. Ahmad, Surface passivation of perovskite layers using heterocyclic halides: improved photovoltaic properties and intrinsic stability, Nano Energy 50 (2018) 220–228.
[48] H. Dong, Z. Wu, J. Xi, X. Xu, L. Zuo, T. Lei, X. Zhao, L. Zhang, X. Hou, A.-K.-Y. Jen, Pseudohalide-induced recrystallization engineering for CH3NH3PbI3 film and its application in highly efficient inverted planar heterojunction perovskite solar cells, Adv. Funct. Mater. 28 (2018) 1704836.
[49] J. Guo, B. Wang, D. Lu, T. Wang, T. Liu, R. Wang, X. Dong, T. Zhou, N. Zheng, Q. Fu, Z. Xie, X. Wan, G. Xing, Y. Chen, Y. Liu, Ultralong carrier lifetime exceeding 20 μS in lead halide perovskite film enable efficient solar cells, Adv. Mater. 35 (2023) 2212126.
[50] Y. Li, W. Xu, N. Mussakhanuly, Y. Cho, J. Bing, J. Zheng, S. Tang, Y. Liu, G. Shi, Z. Liu, Q. Zhang, J.R. Durrant, W. Ma, A.W.Y. Ho-Baillie, S. Huang, Homologous

bromides treatment for improving the open-circuit voltage of perovskite solar cells, Adv. Mater. 34 (2022) 2106280.
[51] M.V. Khenkin, E.A. Katz, A. Abate, G. Bardizza, J.J. Berry, C. Brabec, F. Brunetti, V. Bulović, Q. Burlingame, A. Di Carlo, R. Cheacharoen, Y.-B. Cheng, A. Colsmann, S. Cros, K. Domanski, M. Dusza, C.J. Fell, S.R. Forrest, Y. Galagan, D. Di Girolamo, M. Grätzel, A. Hagfeldt, E. von Hauff, H. Hoppe, J. Kettle, H. Köbler, M.S. Leite, S. Liu, Y.-L. Loo, J.M. Luther, C.-Q. Ma, M. Madsen, M. Manceau, M. Matheron, M. McGehee, R. Meitzner, M.K. Nazeeruddin, A.F. Nogueira, Ç. Odabaşı, A. Osherov, N.-G. Park, M.O. Reese, F. De Rossi, M. Saliba, U.S. Schubert, H. J. Snaith, S.D. Stranks, W. Tress, P.A. Troshin, V. Turkovic, S. Veenstra, I. Visoly-Fisher, A. Walsh, T. Watson, H. Xie, R. Yıldırım, S.M. Zakeeruddin, K. Zhu, M. Lira-Cantu, Consensus statement for stability assessment and reporting for perovskite photovoltaics based on ISOS procedures, Nat. Energy 5 (2020) 35–49.
[52] W. Tress, M. Yavari, K. Domanski, P. Yadav, B. Niesen, J.P. Correa Baena, A. Hagfeldt, M. Graetzel, Interpretation and evolution of open-circuit voltage, recombination, ideality factor and subgap defect states during reversible light-soaking and irreversible degradation of perovskite solar cells, Energ. Environ. Sci. 11 (2018) 151–165.
[53] W.-H. Chiu, Y.-K. Huang, S.-H. Chen, M.-C. Wu, G. Chen, K.-M. Lee, Exploring the efficiency enhancement of perovskite solar cells by chemical bath depositing SnO2 on mesoporous TiO2 electrode, Mater. Today Chem. 41 (2024) 102329.